LASER POLISHING OF ADDITIVELY MANUFACTURED Ti-6Al-4V – MICROSTRUCTURE EVOLUTION AND MATERIAL PROPERTIES

Paper #054

Juliana S. Solheid[1], Sankhya Mohanty[2], Mohamad Bayat[2], Torsten Wunsch[3], Peter G. Weidler[4]
Hans J. Seifert[1], Wilhelm Pfleging[1,5]

[1]Institute for Applied Materials-Applied Materials Physics, Karlsruhe Institute of Technology, P.O. Box 3640, 76021 Karlsruhe, Germany
[2]Department of Mechanical Engineering, Technical University of Denmark, building 425, Lyngby, Denmark
[3]Institute for Micro Process Engineering, Karlsruhe Institute of Technology, P.O. Box 3640, 76021 Karlsruhe, Germany
[4]Institute of Functional Interfaces, Karlsruhe Institute of Technology, P.O. Box 3640, 76021 Karlsruhe, Germany
[5]Karlsruhe Nano Micro Facility, H.-von-Helmholtz-Platz 1, 76344 Egg.-Leopoldshafen, Germany

Abstract

Laser polishing of metals consists of irradiating the part's surface with a laser beam, thus generating a molten layer that is redistributed and resolidified to create a surface with reduced roughness. However, the process is also characterized by an instantaneously formation of heat-affected zones with consequent microstructural changes that influences the mechanical properties. In order to understand the microstructural evolution during laser polishing of Ti-6Al-4V laser-based powder bed fusion samples, a thermal model is applied in the current study to predict the dimensions of the melted zones and the heat-affected areas. Furthermore, the results obtained through the simulations are discussed and compared to the experimental data, thereby establishing the validity of the process models. Finally, the experimental studies also include the evaluation of the material hardness and residual stresses after laser polishing.

Introduction

The variety of applications for parts produced by additive manufacturing (AM) is growing with the steady improvement of the AM technologies [1]. Laser-based powder bed fusion (L-PBF) is one of the established AM methods for building metallic parts. Despite many advantages, the L-PBF process is not always capable of providing parts that are ready for use. Often the issue is the low surface quality of the resulting parts, which can present high roughness and porosity levels, thus affecting negatively mechanical properties. Surface roughness and pores can cause crack formation during fatigue load [2,3].

Laser polishing (LP) is one possibility of post-processing focused on improving the surface quality of AM parts. The process consists of the ablation and/or remelting of the surface through laser radiation, which is redistributed to create a smoother surface [4,5]. However, the high temperatures achieved during LP can cause extended heat affected zones with consequent microstructural changes that influences the mechanical properties [6,7]. For a well-informed decision regarding the set of laser and process parameters to adopt during the LP process and/or the suitable sequencing of LP within the AM process chain, it is important to understand the type of material modification and underlying mechanisms.

One way of analyzing the surface modifications of the parts during LP while saving material and time is through reliable models. Several approaches have been investigated for the development of accurate models of the LP process. These approaches range from numerical heat transfer combined with fluid flow models to surface predictions considering the asperity of the initial surface and the capillary flow [8-10]. However, models of such complexity can require a great computational time and capacity.

In this work, an investigation of the resulting microstructure and mechanical properties of AM parts submitted to LP is presented. A straight-forward thermal model is adopted for the fast assessment of the melting depths and the heat affected zones, and experimental studies with Ti-6Al-4V samples are performed for validation of the models and for the analysis of the impact of LP on material hardness and residual stresses. The goal is to provide the ability to use the data obtained from numerical and experimental studies to select the LP process parameters according to the requirements and limitations of the mechanical properties.

Modelling

Heat Transfer Model

The thermal conditions assumed in the heat transfer model adopted in this work are schematically represented in Figure 1. The laser beam is assumed to be a focused surface heat source that scans the top surface. The top and side surfaces exchange heat with the environment through convection and radiation, while the bottom surface is considered adiabatic. The process simulations were performed on COMSOL Multiphysics 5.4.

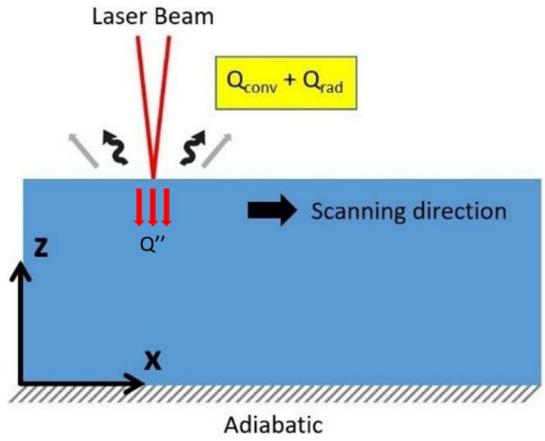

Figure 1 Schematic drawing of the boundary conditions for the applied heat transfer model

The geometry of the used model is presented in Figure 2. The entire domain has dimensions of 12x4x2 mm³, while the domain scanned by the laser beam has dimensions of 6x1x1 mm³. The maximum mesh element size along the laser affected area is 10^{-4} m.

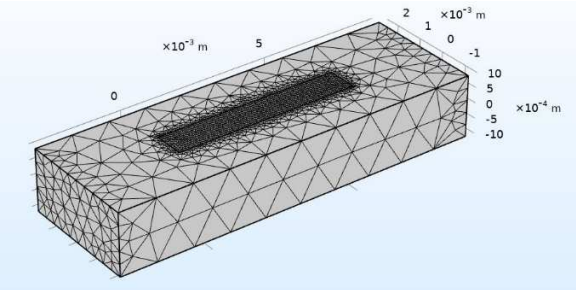

Figure 2 Geometry and mesh distribution of the present model

The governing heat transfer equation is expressed in Equation (1),

$$\rho C_p \frac{\partial T}{\partial t} = k\nabla^2 T \quad (1)$$

where k is the effective thermal conductivity, C_p and ρ are the effective specific heat capacity and density of the material, respectively.

The convection and radiation heat transfer between the side and top surfaces can be described by Equation (2) and (3), respectively,

$$Q_{conv} = h(T_{amb} - T) \quad (2)$$

$$Q_{rad} = \varepsilon\sigma(T_{amb}^4 - T^4) \quad (3)$$

with h the convective heat transfer coefficient, ε and σ the surface emissivity and the Stefan-Boltzman constant, respectively.

Q'' is the surface heat generation term and is expressed as a Gaussian heat flux as shown is Equation (4),

$$Q'' = \frac{2\alpha P_w}{\pi R_w^2} e^{\frac{-2(x^2+y^2)}{R_w^2}} \quad (4)$$

R_w is the distance from the centre of the heat source, α is the laser absorption coefficient and P_w is the laser power. The values adopted for the described thermo-physical properties and simulated process parameters are presented in Table 1.

Table 1 Thermo-physical properties of Ti-6Al-4V and simulated process parameters [11-13]

Property	Value
Density (ρ)	4000 kg/m^3
Solidus temperature (T_s)	1878 K
Liquidus temperature (T_l)	1928 K
Specific heat capacity, solid phase (C_{ps})	543 J/kg K
Specific heat capacity, liquid phase (C_{pl})	770 J/kg K
Thermal conductivity, solid phase (k_s)	13 W/m K
Thermal conductivity, liquid phase (k_l)	80 W/m K
Laser absorption coefficient (α)	0.3
Laser Power (P_w)	300 W
Average scanning speed (v)	1200 mm/s
Hatch distance (h_d)	50 µm

The fluid flow during melting has a great influence on the heat dissipation physics and, consequently, on the maximum temperatures achieved during the process

[14]. However, in order to maintain the computational time low, the fluid flow is not directly considered. Instead, the value of the liquid thermal conductivity is adapted so the obtained melting and HAZ depths reflect the reality of the experiments.

Experimental setup

Material

The starting material investigated in this work were Ti-6Al-4V blocks manufactured via L-PBF. The samples were analyzed in three conditions: after the AM process, after heat treatment for stress relief, and after sandblasting. The chemical composition of the material is presented in Table 2.

Table 2 Chemical composition (wt.%) of assessed Ti-6Al-4V produced by L-PBF

Ti	Al	V	C	N	O
87.5	6.4	3.9	0.01	0.001	0.1

The laser post-processing was performed on the side (vertical) surfaces of the AM samples, where a high roughness due to the attachment of powder and the effects from the layer-by-layer building process was obtained (Figure 3). The LP was executed ex-situ, with the parts being removed from the AM machine and processed in a separate laser system.

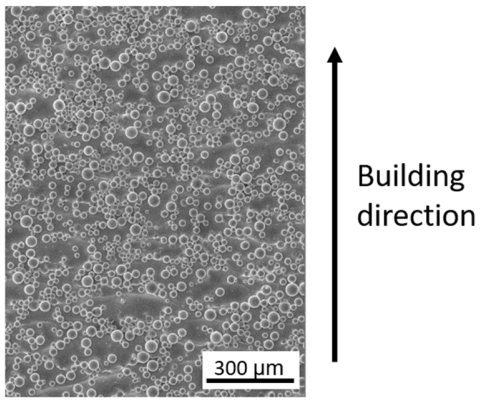

Figure 3 SEM image of the side surface of Ti-6Al-4V AM part

Laser System

For the laser polishing process, a combination of a TruCell 3010 machine and TruDisk 3001 radiation source (TRUMPF GmbH, laser wavelength 1064 nm) were used, which operates in cw (continuous wave) mode. The laser beam is focused onto the sample's surface by lenses BEO D70 with focal length of 150 mm. During the process, a flow of Argon gas was blown on the surface of the sample by a single nozzle in order prevent oxidation of the material. The parameters adopted during the laser polishing experiments are presented on Table 3.

Table 3 Laser polishing parameters

Parameter	Value
Beam diameter	100 µm
Power	300 W
Pendulum frequency	100 Hz
Amplitude	3 mm
Axis federate	0.6 m/min
Processing length	15 mm
Argon flow rate	10 l/min

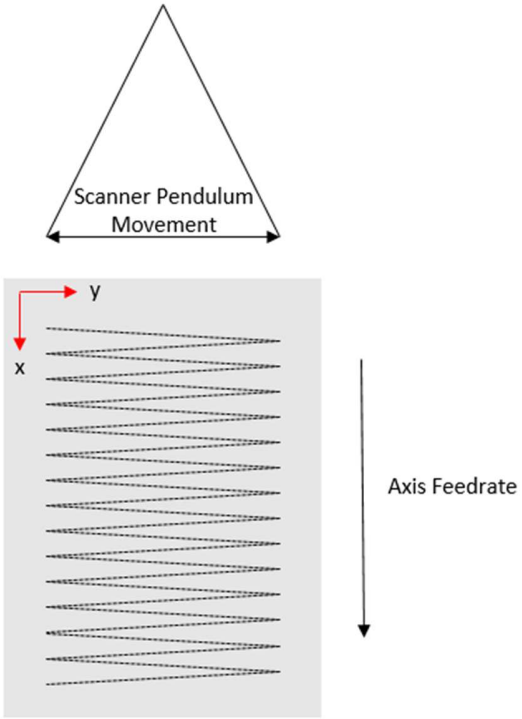

Figure 4 Schematic view of the laser scanning system used during laser polishing

The scanning system works with a pendulum movement (Figure 4) and common parameters such as average scanning speed and hatch distance are not directly input in the machine. For comparing the simulations and experiments, it is necessary to calculate the average scanning speed and the hatch distances. The average scanning speed is the product of the pendulum frequency and four times the amplitude. As for the average hatch distance, it is necessary to first obtain the processing time by dividing the processing length and the axis feedrate and subsequently calculate how much the laser travelled in x-direction between each scanning

line. It is known that the laser scans one line every 0.05 seconds, based on this value and the processing time it is possible to obtain the number of lines for the entire process and subsequently use the number of lines and the processing length to calculate the average distance between each line.

Results and discussion

Melting and Heat Affected Zone

The first experiments for the validation of the thermal model using the properties and parameters described in Table 1 consisted of the analysis of single tracks. The temperatures obtained during the simulation of the process reached a maximum value of 3500 K (Figure 5) which exceeds the melting (1659.85 °C) and boiling (2862 °C)temperature of Ti-6Al-4V [15]. From the cross-section of an experimental single track, it is possible to observe the depths of the melting and heat affected zones (Figure 6).

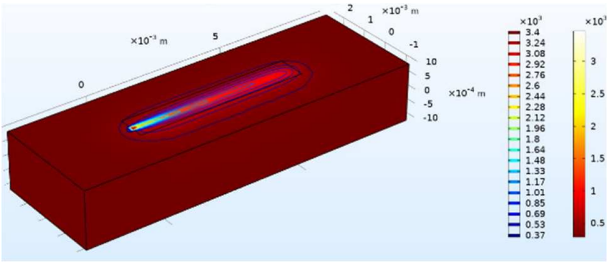

Figure 5 Results of numerical simulation of temperatures obtained during laser polishing

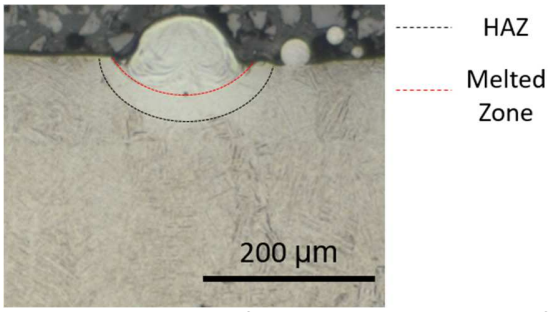

Figure 6 SEM image of the HAZ and melted area of a single track experiment

When comparing the results obtained with the numerical simulation, it is possible to observe that the predicted melting and heat affected zone's shape and depth are very close to the three experimental results performed (Figure 7). The sharp effects on the simulated contours are an effect of coarseness of the mesh – and a smoother more conforming profile is obtained with finer mesh but with significantly higher computing efforts. The current mesh was selected as it could make the prediction within the desired level of accuracy for this study.

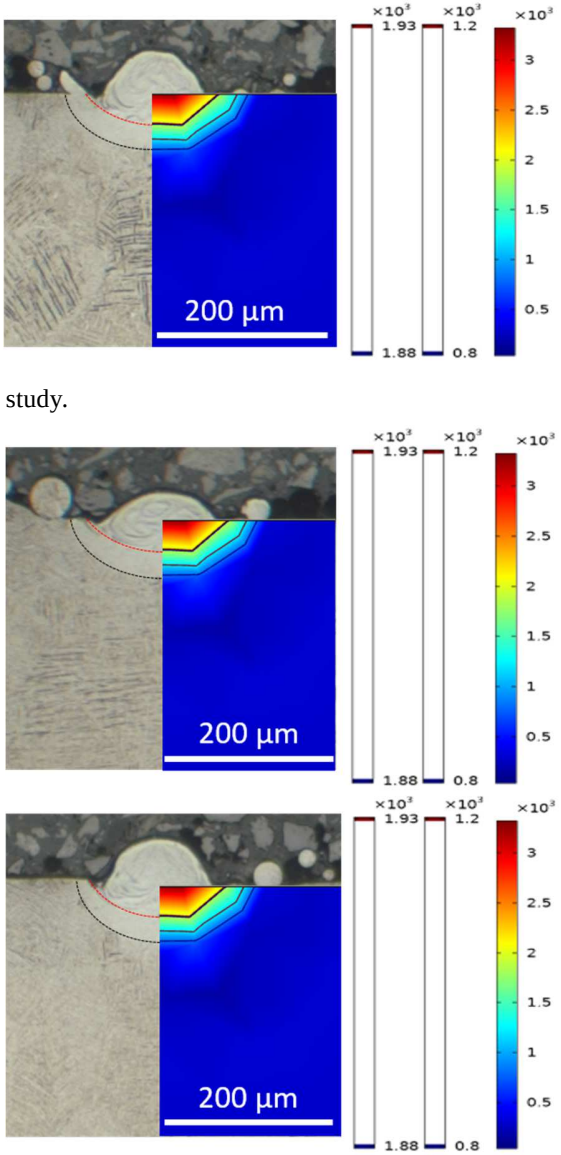

Figure 7 Comparison of the simulated and experimental depths of the melting and heat affected zones

After analyzing the experimental melting and heat affected zones of the single tracks and validating the proposed model, areal experiments were performed with the parameters presented in Tables 1 and 2. The experiments were performed with the same parameters for the samples with the three initial conditions mentioned: as-built (AB), heat treated for stress relief (HT), and sand blasted after heat treatment (SB). The surface texture after the LP presented a clear

improvement when compared to the same surface directly after AM, with Ra values of 6.9 µm before LP (Figure 8) and 5.2 µm after one repetition of the parameter set adopted (Figure 3). By repeating the operation three times in the same area, the surface roughness achieved was 0.8 µm.

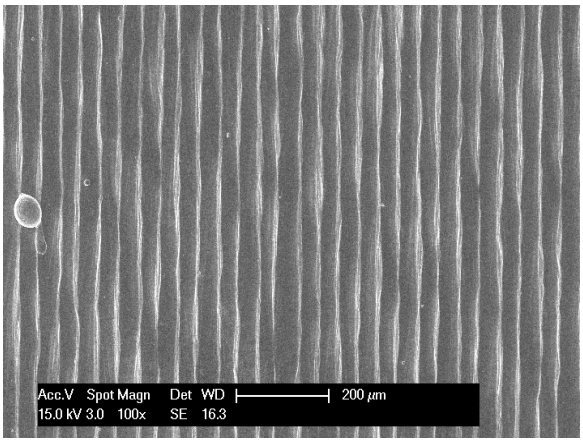

Figure 8 SEM image of the surface after laser polishing

The combination of the HAZ and melting zones can be clearly observed in the HT and SB samples (Figure 9c and 9d), due to the contrasting etching of the metastable α´ phase of Ti-6Al-4V formed in the melting zone against typical α-β phase in the rest of the sample (obtained during the heat treatment after L-PBF). Due to similar high thermal gradients and cooling rates during L-PBF and LP, the overall AB sample also shows martensitic α´ phase formation, and therefore, the HAZ and melting zones of LP cannot be clearly distinguished (Figure 9b).

For the areal experiments, the HAZ plus melting zones had an average depth of 100 µm, while for both the numerical and experimental single lines it was in the range of 70 µm. The different values obtained after the single track and the areal experiments is due to the 50% overlap between the laser tracks during the areal experiments, causing the part to be submitted to more heat over time.

From the presented model, it is possible to obtain different thermal data during the LP process, such as maximum and minimum temperatures, thermal gradients, and cooling rates. In ongoing work the present thermal model is coupled with a metallurgical model to obtain predictions for grain morphology and phase fraction [16,17]. However, these studies are beyond the scope of the presented paper which is focused on the prediction of the laser affected zones and the experimental aspects of the material characterization throughout different steps of the manufacturing process chain.

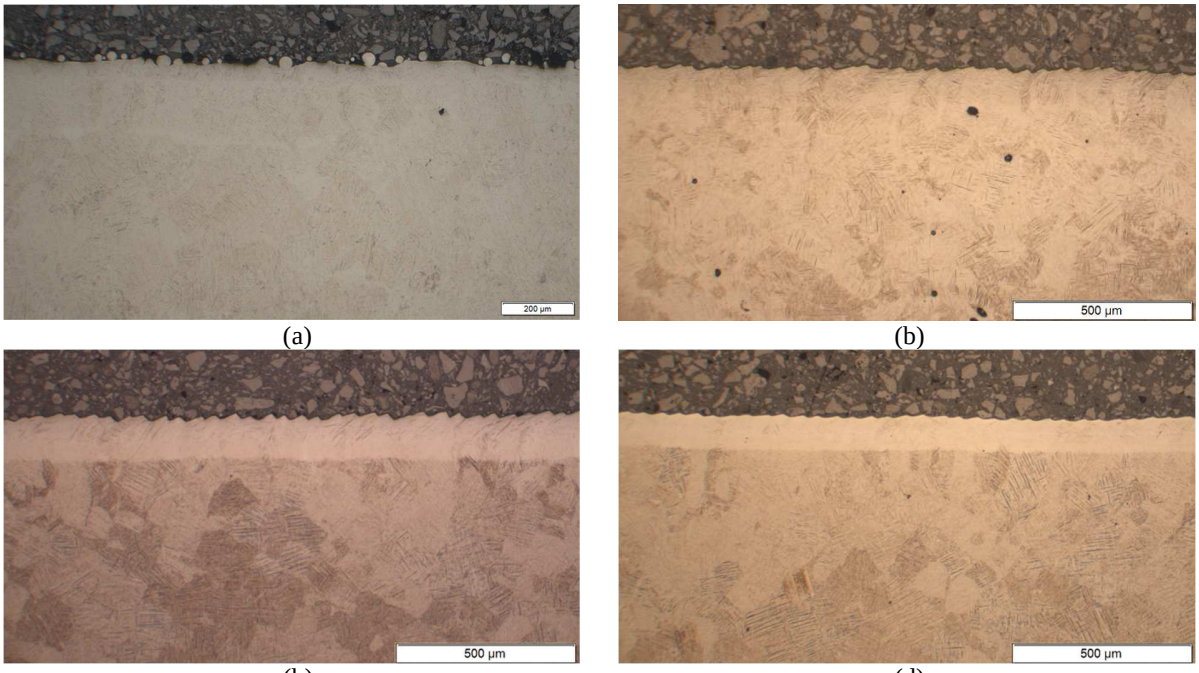

Figure 9 Cross section analysis of the HAZ of: (a) AB sample before LP, (b) AB sample after LP areal experiments, (c) HT sample after LP areal experiments and (d) SB sample after LP areal experiments

Phase analysis

In order to confirm the presence of the expected phases on the samples in the three initial conditions and on the same conditions after LP, XRD analysis was performed.

The patterns obtained for the three initial conditions prior to LP confirmed a majority presence of peaks from the hexagonal (hcp) α phase for the HT and SB samples, while only peaks of the martensitic α´ phase were identified for the AB sample (Figure 10). Both α and α´ phases present a hexagonal crystalline structure but they differentiate from each other by the higher residual stress state on the martensitic α´ microstructure. This difference is represented in the XRD patters as a slight shift on the 2θ angle and as the broadening of the peaks. The remaining peaks observed on the HT and SB samples correspond to the body-centered cubic (bcc) ß phase.

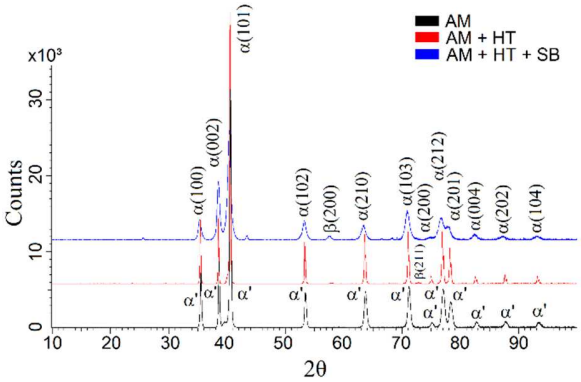

Figure 10 XRD patterns of AB (AM), HT and SB samples

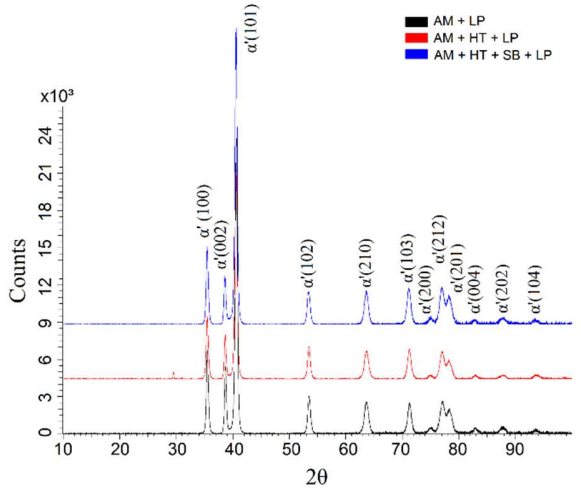

Figure 11 XRD patterns of the samples: AB (AM), HT and SB after LP

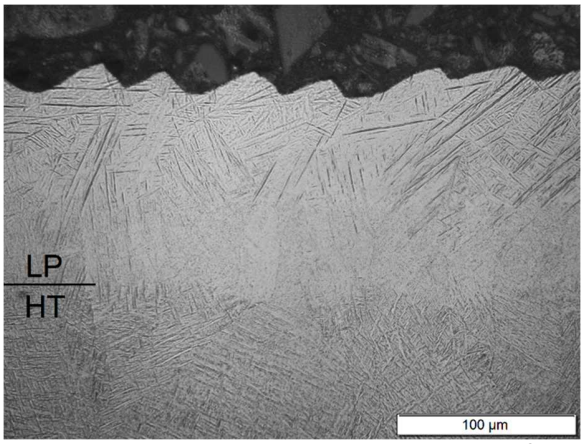

Figure 12 Cross section analysis: optical image of Ti-6Al-4V microstructure after LP (top) and HT (bottom)

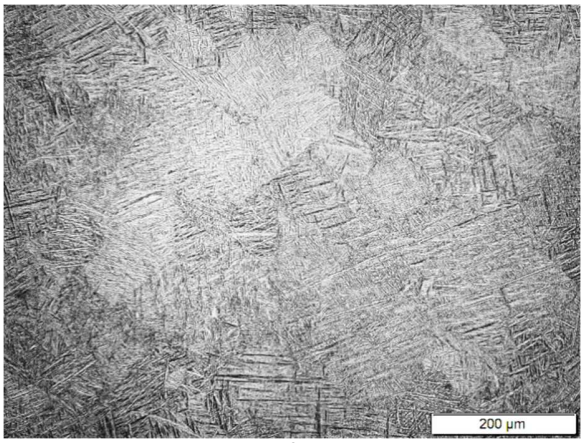

Figure 13 Optical image of Ti-6Al-4V microstructure after heat treatment indicating the presence of α (brighter areas) and ß (darker areas) phases

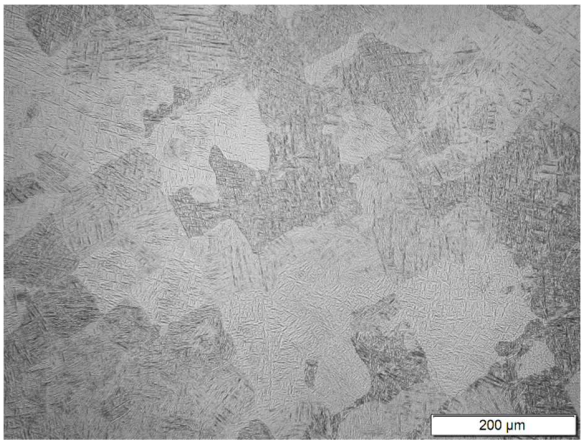

Figure 14 Optical image of Ti-6Al-4V microstructure after additive manufacturing with the presence of only α´ phase

The patterns obtained for the three initial conditions after the LP process presented the exact same peaks for all cases, which indicates the matches the pattern of only α´ phase after laser polishing, with the peak locations and broadening as described above (Figure 11).

The differences between the microstructures can also be confirmed via optical microscopy analysis, in which the martensitic structure on the laser polished and additive manufactured areas present a thin and elongated needle like geometry (Figures 12 and 13) while the microstructure after heat treatment present a lamellar characteristics (Figures 12 and 14).

Residual Stresses

As mentioned in the previous sections, the stress states of the material varies according to which process it was subjected. To quantify the residual stresses of the analyzed samples in the initial conditions and after LP, the Williamson-Hall plot was used, which relates the peak width and Bragg angle obtained with the XRD analysis to the crystallite size and lattice strain [18].

As expected the heat treated sample (HT) presented small ε_0 value (Figure 15). Despite the heat treatment, the SB sample presented a higher stress state, which can be related to compressive stress caused by the sand particles jet on the material´s surface following the stress relief treatment. The samples submitted to LP presented similar ε_0 values for different initial conditions of residual stress, which were between the heat treated and additively manufactured values. Apart from the similarities of the AM and LP processes, the residual stress in the sample analyzed after the additive manufacturing process presented the highest ε_0 value among all samples.

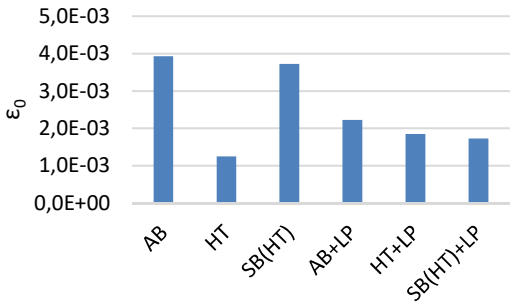

Figure 15 Residual stresses of Ti-6Al-4V samples after different steps of the manufacturing process

Hardness

The change in microstructure and the different stress conditions also have their implications on the mechanical properties of the parts.

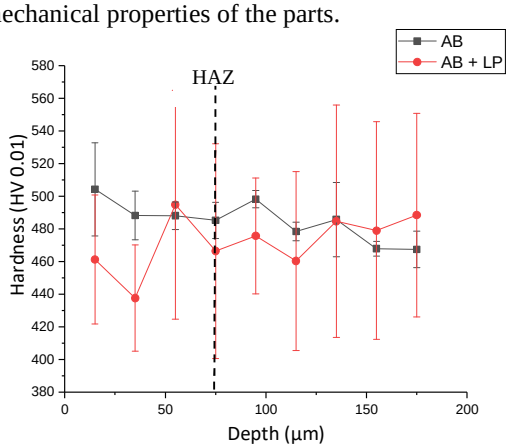

(a)

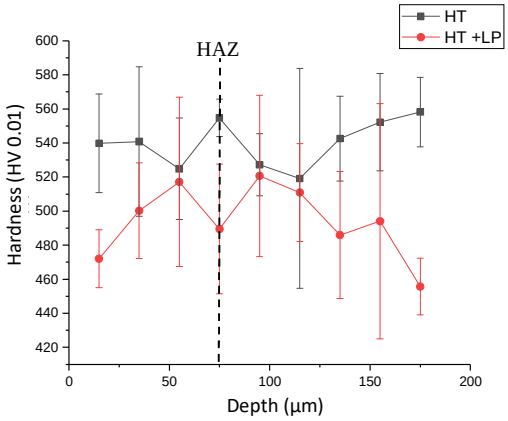

(b)

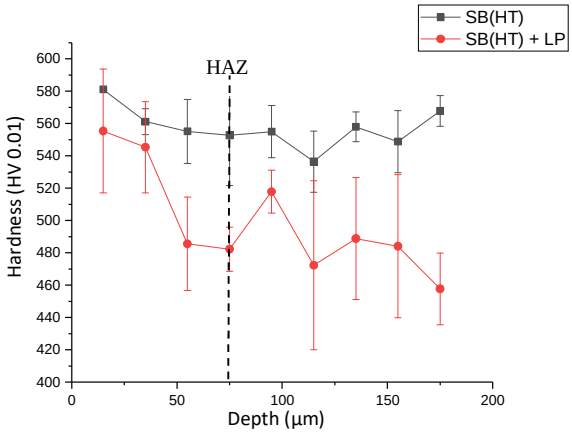

(c)

Figure 16 Vickers micro hardness of Ti-6Al-4V samples before and after laser polishing: (a) AB samples, (b) HT samples and (c) SB(HT) samples

The martensitic α´ microstructure is known to present higher values of hardness when compared to α and ß phases. Although, even with the presence of only α´ phase after the laser polishing, the values obtained from the Vickers micro hardness showed a decrease of the hardness when compared to the HT and SB samples (Figure 16).

This effect on the hardness can be caused by defects generated during the laser polishing process, i.e. cracks or pores, but these defects were not observed in the LP samples. The magnitude of the error bars and the deviation of the values, even among the laser polished samples, suggest a limitation regarding the repeatability of the measurement system. Furthermore, the expected evident difference on the hardness of the laser polished samples within the HAZ (up to 100 µm) and beyond (over 100 µm) is not observed in the current measurement results.

Conclusions

In this work, the analysis of the microstructure evolution and selected mechanical properties for L-PBF Ti-6Al-4V samples in different steps of the process chain was presented together with a heat transfer model for the prediction of the depths of HAZ and melting zone.

In their initial conditions, the samples presented two different types of microstructure, being all α´ phase for the samples analyzed straight after the AM process and a combination of α and ß phases for the samples submitted to stress relief heat treatment. After the laser polishing, all samples presented the same microstructure evolution with the presence of only the α´ phase. The stress state of the samples after the laser polishing had a significant variation from the initial conditions. The post-process induced stress in the heat treated samples and acted as a localized stress relief mechanism on the surface of the as-built samples.

With the understanding of the changes that occur in the material in the laser affected areas and with a computational model that can rapidly estimate the depth of these zones, it is possible to make a more informed decision about the suitability of the laser polishing based on each part´s specific requirements.

Acknowledgments

This work has received funding from the European Union's programme PAM^2 within Horizon 2020 under grant agreement No. 721383. The authors would like to thank 3D Systems Leuven to provide samples produced on DMP Flex 350 machine using LaserForm Ti Gr23 (A). Furthermore, the support for laser materials processing by the Karlsruhe Nano Micro Facility (KNMF, http://www.knmf.kit.edu/), a Helmholtz research infrastructure at the Karlsruhe Institute of Technology (KIT), is gratefully acknowledged.

References

[1] Chen L, He Y, Yang Y, Niu S, Ren H. The research status and development trend of additive manufacturing technology. International Journal of Advanced Manufacturing Technologies 2017;89:3651-3660.

[2] Zhang B, Li Y, Bai Q. Defect formation mechanisms in selective laser melting: A review. Chinese Journal of Mechanical Engineering 2017;30:515-527.

[3] Wycisk E, Solbach A, Siddique S, Herzog D, Walther F, Emmelmann C. Effects of defects in laser additive manufactured Ti-6Al-4V on fatigue properties. Physichs Procedia 2014;56:371-378.

[4] Kumstel J, Kirsch B. Polishing Titanium- and Nickel-based alloys using cw-laser radiation. Physics Procedia 2013;41:362-371.

[5] Zhihao F, Libin L, Longfei C, Yingchun G. Laser polishing of additive manufactured superalloy. Procedia CIRP 2018;71:150-154.

[6] Ma CP, Guan YC, Zhou W. Laser polishing of additive manufactured Ti alloys. Optics and Laser in Engineering 2017;93:171-177.

[7] Wang WJ, Yung KC, Choy HS, Xiao TY, Cai ZX: Effects of laser polishing on surface microstructure and corrosion resistance of additive manufactured CoCr alloys. Applied Surface Science 2018;443:167-175.

[8] Marimuthu S, Triantaphyllou A, Antar M, Wimpenny D, Morton H, Beard M. Laser polishing of selective laser melted components. International Journal of Machine Tools and Manufacture 2015;95:97-104.

[9] Shao TM, Hua M, Tam HY, Edmund, Cheung EHM. An approach to modelling of laser polishing of metals. Surface & Coatings Technology 2005;197:77-84.

[10] Wang Q, Morrow JD, Ma C, Duffie NA, Pfefferkorn FE. Surface prediction model for thermocapillary regime pulsed laser micro polishing of metals. Journal of Manufacturing Processes 2015;20:340-348.

[11] Yan W, Qian Y, Wenjun G, Lin S, Liu WK, Lin F, Wagner GJ. Meso-scale modeling of multiple-layer fabrication process in selective electro beam melting: inter-layer/track voids formation. Materials and Design 2018;141:210-219.

[12] Parry L, ashcroft IA, Wildman RD. Understanding the effect of laser scan strategy on residual stress in selective laser melting through thermo-mechanical simulation. Additive Manufacturing 2016;12:1-15.

[13] Huang Y, Yang LJ, Du XZ, Yang YP. Finite element analysis of thermal behaviour of metal powder during selective laser melting. International Journal of Thermal Sciences 2016;104:146-157.

[14] Bayat M, Mohanty S, Hattel JH. A systematic investigation of the effects of proces parameters on heat and fluid flow and metallurgical conditions during laser-based powder bed fusion of Ti6Al4V alloy. International Journal of Heat and Mass Transfer 2019;139:213-230.

[15] Wu H, Ma J, Meng Q, Jahan M.P, Alavi F. Numerical modeling of electrical discharge machining of Ti-6Al-4V. Procedia Manufacturing 2018;26:359-371.

[16] De Baere D, Bayat M, Mohanty S, Hattel J. Thermo-fluid-metallurgical modelling of the selective laser melting process chain. Procedia CIRP 2018;74:87-91.

[17] Bruyere V, Touvrey C, Namy P, Authier N. Multiphysics modeling of pulsed laser welding. Journal of Laser Applications 2017;29:022403-1-7.

[18] Williamson GK, Hall WH. X-Ray line broadening from filed Aluminium and Wolfram. Acta Metallurgica 1953;1:22-31.